Journal of Materials Science: Materials in Electronics (2018) 29:19013–19027
https://doi.org/10.1007/s10854-018-0027-8

Enhanced field emission from copper nanowires synthesized using ion track-etch membranes as scaffolds

Rashi Gupta[1] · R. P. Chauhan[2] · S. K. Chakarvarti[2] · M. K. Jaiswal[3] · D. Ghoshal[4] · S. Basu[4] · S. Suresh[4] · Stephen F. Bartolucci[5] · N. Koratkar[4,6] · Rajesh Kumar[1,4]

Received: 6 June 2018 / Accepted: 6 September 2018 / Published online: 11 September 2018

Abstract

Copper nanowires have been synthesized at different pH values through the template assisted electrodeposition technique using polycarbonate track-etch membranes as scaffolds. The effect of pH (0.8–2.8) of the electrolyte on structure, morphology, composition and deposition rate of copper into the pores of the template, while keeping other electrochemical conditions same, was investigated. X-ray diffraction analysis confirmed the face centered cubic phase of synthesized nanowires. With the change in pH, no shift in peaks was observed except the inclusion of an additional peak of copper oxide in nanowires synthesized at pH 2.8. The nanocrystallite size, strain, lattice stress and energy density were evaluated by X-ray analysis. Field emission scanning electron microscopy images revealed that nanowires obtained at pH 0.8, 1.1 and 1.4 showed incomplete deposition in the pores of the membrane whereas, the nanowires obtained at pH 1.7 were densely stacked, vertically aligned and uniform along the diameter and that obtained from pH 2.0–2.8 had overdeposition on their top. An increase in deposition rate was observed with the increase in pH value. The average diameter of Cu nanowires was found to be ~ 105 nm. The electrical conductivity of as-grown nanowires was observed to decrease 13-fold as the transition from bulk values to the nanosystem. Nanowires prepared at pH of 1.7 were characterized for their field-emission properties. A very large field-enhancement factor of ~ 10,855 was obtained indicating that Cu nanowires grown by reported technique shows outstanding potential as efficient field-emitters for flat panel displays.

1 Introduction

Low dimensional structures have received attention owing to their unusual and enthralling properties compared to that at the bulk level. Immense opportunities can be perceived by downsizing the structures into lower dimensions. Confinement of electrons show size dependent excitation and emission [1], ballistic conductance [2] and single electron tunneling [3]. Such minuscule structures can be synthesized using hydrothermal [4], sol–gel [5], sonochemical [6], electrodeposition [7–11] and other techniques.

The synthesis techniques of low-dimensional structures are broadly categorized into two types (1) top–down (2) bottom–up approach. The bottom–up approach is most popular as it offers unparalleled control over the morphology of nanoparticles [12–15]. One dimensional structures like ribbons, rods, cones, wires etc. are being extensively studied due to their application in mesoscopic physics and modeling of nanolevel devices [16]. They are used as interconnects and functional units of small-scale devices [17], diode junctions [18] and sensing applications [19]. In particular, 1D

✉ Rajesh Kumar
kumarrrpi@gmail.com

[1] University School of Basic and Applied Sciences, Guru Gobind Singh Indraprastha University, New Delhi 110078, India

[2] Department of Physics, National Institute of Technology, Kurukshetra 136119, India

[3] Department of Physics, Shaheed Rajguru College of Applied Sciences for Women, University of Delhi, New Delhi 110096, India

[4] Department of Mechanical, Aerospace and Nuclear Engineering, Rensselaer Polytechnic Institute, Troy, NY 12180, USA

[5] U.S. Army Armaments Research Development and Engineering Center, Benet Laboratories, Watervliet, NY 12189, USA

[6] Department of Material Science and Engineering, Rensselaer Polytechnic Institute, Troy, NY 12180, USA

structures are especially suitable to elucidate the dependence of mechanical, galvanic, optical and thermal properties on dimensionality [20–24].

Although synthetic porous solids are being studied for a long time, yet their fabrication and characterization with definite nano-architectures has been the subject of intense research in recent times. Template-based synthesis offers several advantages over other methods for the synthesis of 1D nanomaterials. These include: (1) mild synthesis conditions [25], (2) fast growth rate, (3) control over the morphology, and (4) ease in the deposition of multilayered materials. Free-standing, aligned and non-aligned nanowires and nanorods could be prepared using a template-based approach. The mainly used templates include anodic alumina membrane (AAM), ion track-etch polycarbonate membrane (PC), co block polymer template, mesoporous materials, carbon nanotubes, zeolites etc. [26–30]. AAM and PC membranes are most commonly used for the synthesis of nanorod or nanowire arrays. Both templates are very convenient for the growth of nanorods by various growth mechanisms, but each type of template also has its disadvantages. The advantages of using PC as the template are its facile handling and removal by means of decomposition at high temperatures or dissolution in a solvent. The template pores can be filled by using capillary forces, electric potential, centrifugation force, and chemical vapor deposition [31, 32]. Electrochemical and electrophoretic deposition both could be done using electric field [33]. Electrochemical deposition includes the oriented diffusion of charged reactive species through a solution when an external electric field is applied, and the reduction of the charged growth species at the deposition surface serving as an electrode. In industry, electrochemical deposition is widely used to coat metals and the process is known as electroplating [34]. In general, this method is only applicable to electrically conductive materials such as metals, alloys, semiconductors, and electrically conductive polymers. When the deposition is confined to the pores of template membranes, nanocomposites like nanorod or nanowire arrays are produced. The growth of nanowires of conducting materials in an electric field is a self-propagating process [35]. Once the small rods form, the electric field and the density of current lines between the tips of nanowires and the opposing electrode are greater than that between two electrodes, due to the shorter distances between the nanowires and the electrodes. This ensures that the species being deposited is constantly attracted preferentially to the nanowire tips, resulting in continued growth. To better control the morphology and size, templates containing channels in the desired shape are used to guide the growth of nanowires. The template is attached to the cathode, which is brought into contact with the deposition solution. The anode is placed in the deposition solution, parallel to the working electrode. When an electric field is applied, cations diffuse through the channels and deposit on the cathode, resulting in the growth of nanowires inside the template. A variation in current density is observed at different stages of deposition when a constant electric field is applied. The current does not change significantly until the pores are completely filled, at which point the current increases rapidly due to improved contact with the electrolyte solution. The current saturates once the template surface is completely covered. The nanowires obtained using this approach were found to be true replicas of the pores [36]. Possin prepared various metallic nanowires using radiation track-etched mica [37]. Williams and Giordano produced silver nanowires with diameters of less than 10 nm [38]. Whitney et al. fabricated arrays of nickel and cobalt nanowires, also using PC templates [39].

Copper being less expensive and abundantly available metal, copper based nanomaterials act as a viable alternative to the rare and expensive metals like silver though its conductivity is 6% less than silver [40]. Thus, copper can be an economically cheap alternative to silver without showing much difference in performance. Copper is a 3*d* transition metal and shows fascinating physical and chemical properties. It exists in many oxidation states which make it suitable for organic transport, photocatalysis, electrocatalysis etc. [41–45]. Copper nanowires can also improve the performance of transmittance networks and electronic systems [46]. The enhanced non-linear optical properties of copper arising due to Plasmon surface resonance phenomenon also makes it useful in optical switches or photochromic glasses [47].

Comprehensive research is being carried out on electron emitters because of their plentiful applications in the field of flat panel arrays, electron beam lithography instruments, vacuum nanoelectronics, cathode ray tube displays accelerators and X-ray sources [48–51]. The electron beam can be generated in metals and semiconductors either by heating at large temperature or by cold field emission [52, 53]. The materials that show high current density and low strength of turn-on electric field are best suited for commercial applications. These requirements can be attained by optimizing the alignment and tip size of the nanostructures. Lately, materials with sharp tips grown on planar substrates show outstanding field emission arising due to local field enhancement on the tips [54, 55]. Chang et al. [56] reported 12.4 V/μm turn-on field for Cu nanopillars of 7 μm length with field enhancement factor as 713. Zhou et al. [57] recorded a very high field enhancement factor of 4400 and a turn on field of 2.2 V/μm for partly aligned Mo nanowires of length 3.1 μm. Wang et al. [58] noticed a field enhancement factor of 1904 for partly aligned Tungsten (W) nanowhiskers of length 20 μm. Deheer et al. [59] reported that tube-tube contact acts as static defect and decreased mean free path of the electrons for carbon

nanotubes of diameter 10 nm and length 1–5 μm aligned parallel to each other.

In this work, we have synthesized Cu nanowire arrays for field-emission applications using the template-based electrochemical deposition at different pH values (0.8, 1.1, 1.4, 1.7, 2.0, 2.3 and 2.8) while keeping other electrochemical and other conditions viz., electrodeposition potential, time, molarity, temperature, pore size unchanged. The structural and morphological properties were studied using XRD and SEM techniques. The Scherrer and Williamson–Hall (W–H) methods were used to evaluate the crystallite size. Also, the electrical properties of the nanowires were studied. There is minimal prior work on the effect of pH on the deposition rate and structural variation in nanowires obtained using template-based electrochemical deposition and field emission. An extremely large field-enhancement factor of > 10,800 was observed for the Cu nanowires (obtained at pH 1.7), which to the best of our knowledge is one of the highest values reported in the literature for field emission from copper nanostructures.

2 Materials and methods

2.1 Chemicals

Copper(II) sulphate pentahydrate ($CuSO_4 \cdot 5H_2O$), Dichloromethane (CH_2Cl_2) and Sulphuric acid (H_2SO_4) (Sigma Aldrich) were demarcated pure. Double distilled water was used throughout the experiments.

2.2 Experimental setup and Cu nanowires synthesis

A two-electrode cell made of Teflon was used to conduct an electrochemical experiment and prepare an array of copper nanowires. A cylindrical copper rod with one end shaped as a cone was used as counter electrode and a polycarbonate TEM with through pores attached to a conducting substrate acted as the working electrode during the deposition process. One-sided adhesive copper tape (3M) was used as conducting substrate for the nucleation of copper grains. This conducting copper tape was further fixed on a curved copper disc working as a cathode with an o-ring fitted in the top enclosure of the cell. Figure 1a represented the 3D diagram of the electrochemical cell used for electrodeposition of Cu nanowires and Fig. 1b shows the schematic of the main steps associated with the fabrication of Cu nanowires using ion track-etch membranes (TEM) as scaffolds. Commercially available polycarbonate TEM (Whatman) with 100 nm pore diameter and 10^6 pores cm^{-2} pore density was used as a scaffold to direct the growth of nanowires. The area in contact with the electrolyte was determined by the inner diameter of the o-ring. The deposition electrolyte consisted of 1.0 M $CuSO_4 \cdot 5H_2O$ prepared using doubled distilled water. No additives or complex reagents were used during the deposition process except the change in the pH values. The electrochemical deposition in all cases of variable pH values was carried out potentiostatically at 0.35 V for 16 min at room

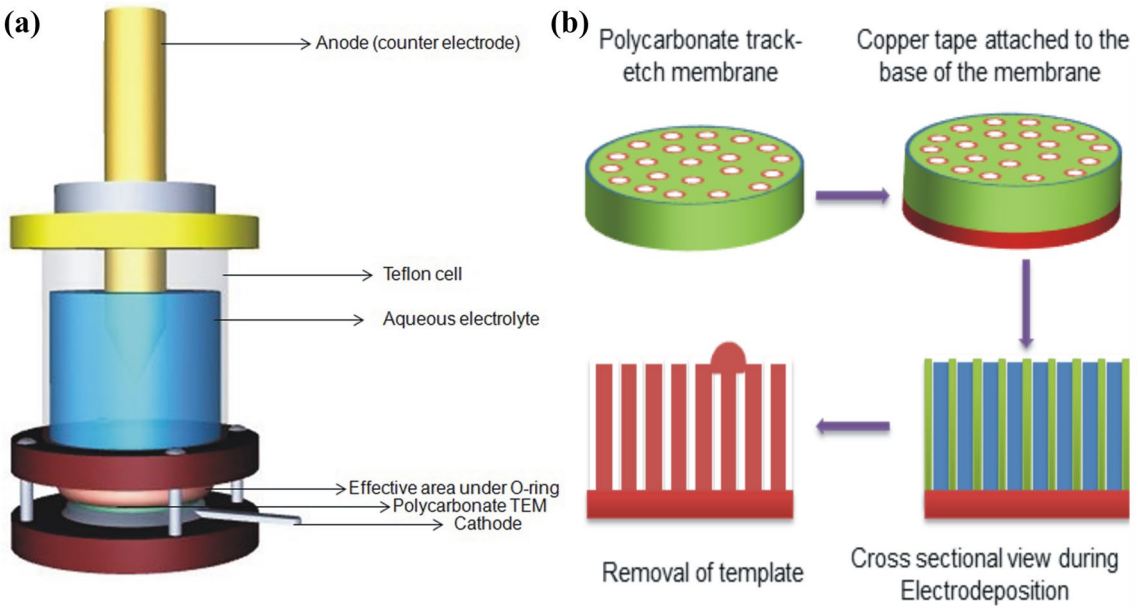

Fig. 1 Schematic representation of **a** electrochemical cell used for electrodeposition of Cu nanowires and **b** main steps associated in the fabrication of Cu nanowires using ion track-etch membranes as scaffolds

temperature (25 °C). The current variation of 0.007–0.011 A was observed during the deposition. The pH of the electrolyte was varied from 0.8 to 2.8 by adding few drops of H_2SO_4 using micropipette. The copper substrate surface was pre-cleaned with 0.1 M H_2SO_4. On the completion of the deposition process, the samples were delicately separated from the cell, rinsed with double distilled water and finally dried in open air. The membrane helped in the protection of samples from direct oxidation. The copper nanowires were harvested by dissolving the template in dichloromethane (CH_2Cl_2).

2.3 Characterization methods

The crystalline structure of the nanowires was investigated by Bruker X-ray powder diffraction with CuK_α wavelength ($\lambda = 1.5406$ Å) operated at 40 kV and 40 mA. All diffract graphs were examined from 30° to 100° with a step size of 0.02°. Field emission scanning electron microscopy (MIRA 7718, TESCAN) was employed to characterize the morphology of the nanowires. The chemical composition of the synthesized samples was analyzed by energy dispersive X-ray spectroscopy. I–V characteristic (IVC) measurements were done using Keithley 2400 source meter. The tungsten tip was used as one electrode in two-electrode set up to make contact with the nanowires embedded in the polycarbonate membrane while Cu base substrate acted as another electrode during the I–V measurements. At a time, the tungsten probe covered around 300 nanowires and the measurements were carried out at different regions of the TEM.

3 Results and discussion

3.1 SEM analysis

FESEM images of copper nanowires deposited using different pH aqueous citrate baths were shown in Fig. 2. As may be seen from FESEM images for pH value 0.8, 1.1 and 1.4 (Fig. 2a, c, d), show incomplete deposition in the pores of the membrane. However, increase in length with an increase in pH is indicated and the nanowires corresponding to pH 1.7 (Fig. 2e, f) were dense, vertically aligned, smooth and with an average diameter 105 nm (as shown in the histogram in Fig. 2b). The variation in wire diameter was measured using ImageJ software for a large data sample of nanowires. Further, increasing the pH value from 1.7 to 2.8, over-deposition in the form of caps was observed in all cases (Fig. 2g for pH 2.8). The well-known chemical reactions depicting the formation of copper nanowires are as follows:

Copper sulphate dissociates into Cu^{+2} and SO_4^{-2} ions in presence of an acidic medium

$$CuSO_4 \rightarrow Cu^{+2} + SO_4^{-2}$$

Under appropriate potential difference Cu^{+2} ions get reduced and generate copper grains starting from the bottom end of the pore, and further continuous growth takes place within the pore due to confinement within the pore boundaries [60].

$$Cu^{+2} + 2e^- \rightarrow Cu$$

Hydrogen gas is liberated at the cathode due to the reduction of the H^+ ions

$$2H^+ + 2e^- \rightarrow H_2$$

As shown in Fig. 3 the deposition process takes place in three steps (1) an electric charge double layer is formed that leads to the reduction of ions at the working electrode, (2) growth within the orifice of the template and (3) over deposition over the ends of the template pores. Firstly, under electrochemical polarization, an electric charge double layer is built-up which forms potential gradient across the length of the scaffold. The potential loss increases along the length from bottom to top due to high electric resistance [61]. As the negative potential is applied to the bottom of the template (Fig. 3a.3) Cu^{+2} ions move towards the bottom of the pores through diffusion [62], where they form copper grains (Fig. 3a.4) due to reduction process which further assembles according to the shape of the template giving rise to nanowires. Once the deposition is complete till the end of the template pore, the reduction no longer takes place through diffusion within the pores; rather the growth starts on the surface of the template. This over-deposition rate is very fast due to the increase in electrode surface area thereby leading to the formation of caps on the top of the nanowires (Fig. 2g).

The aqueous citrate bath at pH 0.8 contains the maximum amount of concentrated sulphuric acid which results in an abundance of H^+ and SO_4^{-2} ions compared to that present at pH 1.7 and 2.8. The slower rate of deposition leading to the incomplete growth of nanowires can be attributed to two reasons (1) excess of H^+ ions (2) excess of SO_4^{-2} ions. Due to excess of H^+ ions the reduction of H^+ is very dominant (Fig. 3b.1), probably leaving very fewer sites on the surface of the working electrode for metal deposition [63]. Excess of SO_4^{-2} ions obstructs the motion of Cu^{+2} ions (Fig. 3b.1), thus decreasing their mean free path resulting into a lesser number of Cu^{+2} ions to diffuse into the pores leading to slow deposition rate of Cu metal. Further, with the increase in pH value from 0.8 to 1.4, the concentration of H^+ and SO_4^{-2} ions decreases leading to increase in length of the nanowires (Fig. 2c, d)

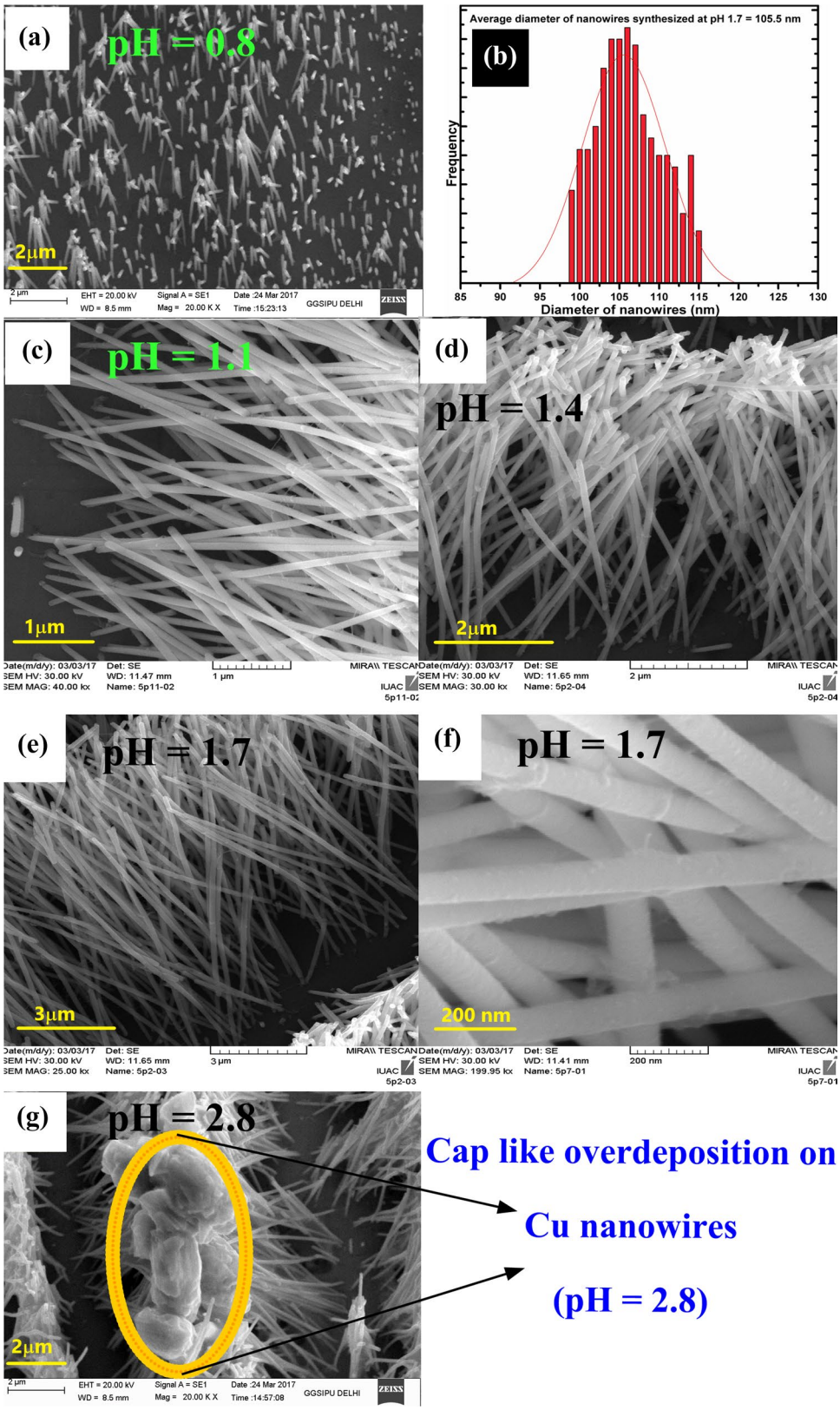

Fig. 2 FESEM images of nanowires obtained from aqueous citrate electrolyte at **a** pH 0.8, **c** pH 1.1, **d** pH 1.4, show incomplete deposition; **e, f** pH 1.7 are dense, vertically aligned, smooth and uniform in diameter and **g** pH 2.8 exhibit over-deposition over the nanowires in the form of caps. **b** Histogram showing the distribution of diameter of Cu nanowires synthesized at pH 1.7 with average diameter of 105 nm

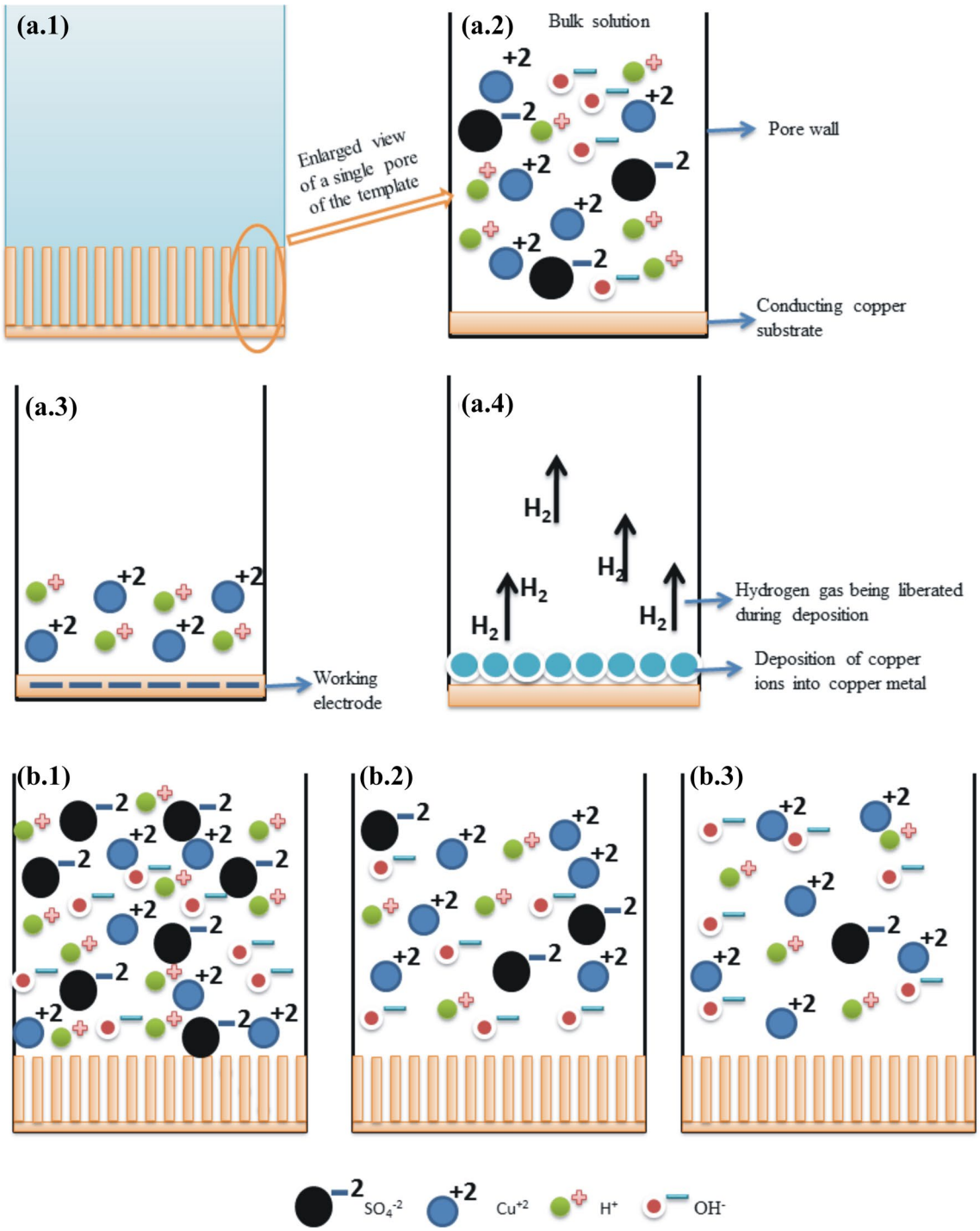

Fig. 3 Schematic representing **a** growth of nanowire within each pore of the template **a.1** cross-sectional view of the template with the electrolyte filled into its pores **a.2** enlarged view of the single pore of the template showing all the ions present in it **a.3** on application of external potential copper tape acts as working electrode and attracts all the copper and hydrogen ions towards itself and **a.4** reduction of copper ions into copper nanograins and hydrogen ions into hydrogen gas and **b** comparative number of ions at pH **b.1** 0.8, **b.2** 1.7 and **b.3** 2.8 that are present in a pore of the template which effects the mean free path of Cu^{+2} ions and hence the deposition rate of copper into the pores of the template

within the same deposition time. At pH 2.8, the concentration of H^+ and SO_4^{-2} ions is the least (Fig. 3b.3) compared to that at pH 0.8 and 1.7. This, therefore, causes lesser collisions amongst the ions leading to increase in the mean free path. It results in faster deposition rate that causes overdeposition in the form of caps (Fig. 2g).

3.2 XRD and EDS analysis

Bruker X-ray diffractometer was used to study the crystallinity, structural phase and lattice parameters. The strain, lattice stress and energy density were evaluated by Scherrer and Williamson–Hall (W–H) methods that are based upon line broadening analysis. XRD analysis (JCPDS 04-0836 and 48-1548) confirmed the face centered cubic phase of synthesized nanowires at pH 0.8–2.8. As there was no significant change in the XRD spectra for pH 1.1, 1.4, 2.0 and 2.3, only the XRD spectra corresponding to pH 0.8, 1.7 and 2.8 i.e. extreme and optimized pH values have been shown in Fig. 4. With the change in pH, no shift in peaks was observed but the inception of copper oxide peak in nanowires synthesized at pH 2.8 revealed that nanowires were oxidized as shown in Fig. 4c. The concentration of OH^- ions was highest at pH

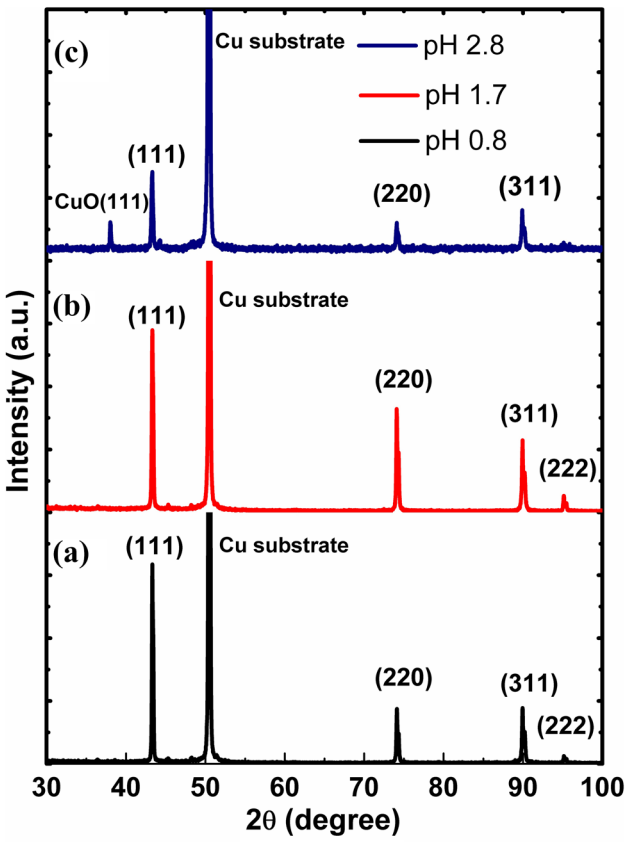

Fig. 4 XRD spectra of Cu nanowires obtained from different aqueous citrate baths having pH **a** 0.8, **b** 1.7 and **c** 2.8

2.8 leading them to react with Cu^{+2} ions and forming copper oxide. The potential–pH equilibrium diagram is used to determine the conditions for deposition of copper oxides at the cathode. The pH of the electrolyte plays a vital role in the deposition of copper oxides [64–66]. Initially, there are lesser number of H^+ ions in the solution compared to that at pH 0.8 and the applied potential is also sufficient enough to induce hydrogen evolution which further reduces the H^+;

$$2H^+ + 2e^- \rightarrow H_2$$

The concentration of OH^- ions increases due to exhaustion of H^+ ions in the form of hydrogen gas. The excess OH^- ions react with the Cu^{+2} leading to the formation of copper hydroxide which further dehydrates and generate more stable copper oxide;

$$Cu^{+2} + 2OH^- \rightarrow Cu(OH)_2$$

$$Cu(OH) \xrightarrow{-H_2O} CuO + H_2O$$

This is also in consistency with our XRD results as shown in Fig. 4c indicating CuO peak. In the present work, 0.35 V potential is applied which also favors the formation of Cu_2O on the working electrode according to the following reactions [64];

$$Cu^{+2} + OH^- + e^- \rightarrow Cu(OH)$$

$$2Cu(OH) \xrightarrow{-H_2O} Cu_2O + H_2O$$

Cu_2O is thermodynamically unstable outside the pH range 6–14 [65]. Cu_2O thus formed gets decomposed and is not present in our polycrystalline nanowires as shown in XRD spectra in Fig. 4. Fullprof program was used for obtaining the refined cell parameters value. The refinement model is required to produce matched peak positions as well as intensities. Figure 5 showed that the observed and calculated patterns are in good agreement. The values of profile R factors determine the goodness of fit (GOF) for peak shape and position, structure and background. The relatively lower values of R_p and R_{wp} are considered for good profile refinement. The refined structural parameters and profile R-factors have been listed in Table 1. The obtained values of R-factors are less than 10%, as well as matching of observed and calculated patterns confirmed the goodness of refinement. From EDS spectrum, the calculated wt% of copper is found to be 97.9% along with a very little oxygen percentage of around 2.02% as shown in Fig. 6.

3.3 Crystallite size and strain

The study was made for the sample synthesized for the optimized pH 1.7.

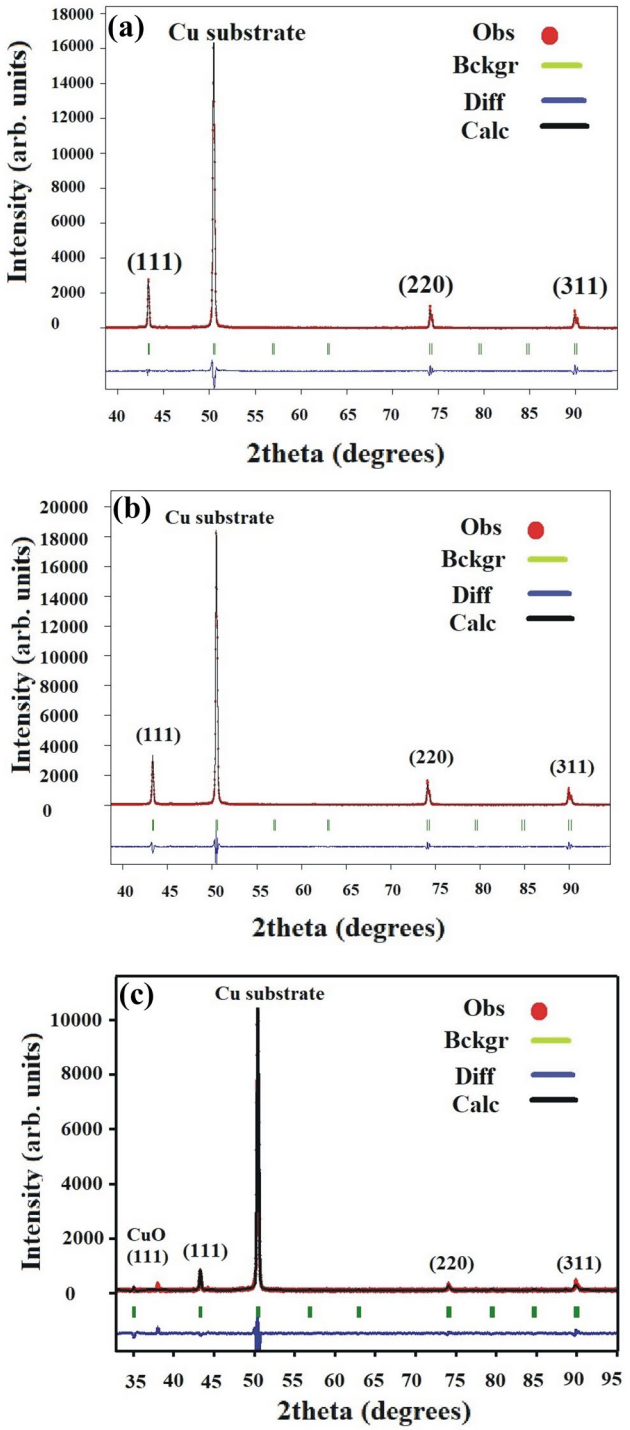

Fig. 5 Refined XRD patterns of copper nanowires obtained from different aqueous citrate baths having pH **a** 0.8, **b** 1.7 and **c** 2.8

3.3.1 Scherrer method

The crystallite size of copper nanowires was determined using line broadening of Bragg peaks. The crystallite size of copper nanowires was calculated using the Debye–Scherrer formula [67–70]:

$$L = \frac{K\lambda}{(\beta_D)_{Measured} cos\theta} \tag{1}$$

where K is constant having a value equal to 0.94, λ is the wavelength of CuKα radiation (1.54056 Å), L is the crystallite size, θ is the Bragg peak position and β_D is the full width of the peak at half the maximum intensity. The actual broadening of the peak is a combination of both instrument and sample effects. A standard reference such as silicon was used to calculate the instrumental broadening. The actual broadening was calculated by subtracting $(\beta_D)_{Instrumental}$ aberration from the measured value $(\beta_D)_{Measured}$ [71].

$$\beta_D = \left[(\beta_D)^2_{Measured} - (\beta_D)^2_{Instrumental} \right]^{1/2} \tag{2}$$

Thus, the corrected formula becomes:

$$L = \frac{K\lambda}{(\beta_D) cos\theta} \tag{3}$$

taking log of Eq. (3);

$$\ln\beta_D = ln\frac{k\lambda}{L} + ln\frac{1}{cos\theta} \tag{4}$$

From the plot between $\ln\beta_D$ and ln 1/cosθ, the crystallite size was estimated by the y-intercept of the line obtained after linear fitting the data points using the relation $L = k\lambda/e^{(intercept)}$. The modified-Scherrer plot is shown in Fig. 7a. The average crystallite size of copper nanowires was calculated as 29 nm.

3.3.2 Williamson–Hall methods

The broadening of peaks also comes from strain arising due to crystal distortion and imperfections which is given by the relation $\varepsilon = \beta_s/\tan\theta$ where ε is lattice strain and β_s is strain-induced peak width [72]. The dependency of peak width arising from crystallite size varies as 1/cosθ as shown in Eq. (3) and that arising from strain varies as tanθ. The broadening due to both is independent of each other and thus, total broadening is given by;

$$\beta_{hkl} = \beta_D + \beta_S \tag{5}$$

$$\beta_{hkl} = \frac{K\lambda}{Lcos\theta} + 4\varepsilon tan\theta \tag{6}$$

Rearranging Eq. (6)

$$\beta_{hkl} cos\theta = \frac{K\lambda}{L} + 4\varepsilon sin\theta \tag{7}$$

Table 1 Refined parameters of nanostructures obtained at pH 0.8, 1.7 and 2.8

Parameters	pH 0.8	pH 1.7	pH 2.8
Crystal system	Cubic	Cubic	Cubic
Cell length a = b = c (Å)	3.6159 (09)	3.6156 (01)	3.6164 (03)
Cell angle α = β = γ (°)	90	90	90
Volume (Å^3)	47.3532	47.2637	47.3001
R_p, R_{wp}, and χ^2	16.9, 21.9, and 4.68	10.5, 14.8, and 3.25	21.8, 22.9, and 4.75

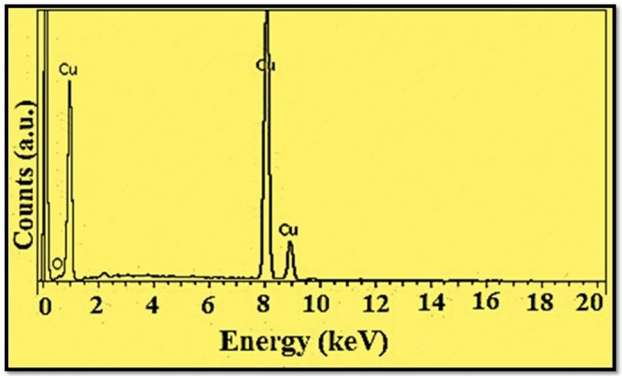

Fig. 6 EDS spectra of Cu nanowires obtained at pH 1.7

Uniform deformation model (UDM) is represented by Eq. (7), in which crystal was considered as isotropic in nature showing uniform strain along all the crystallographic directions. W–H plot was drawn between $\beta_{hkl}\cos\theta$ and $4\sin\theta$ on the x-axis as shown in Fig. 7b. The crystallite size was estimated from the y-intercept of the line obtained after linear fitting the data points using the relation L = kλ/intercept and the strain was equal to the slope of the fitted line.

The uniform stress deformation model (USDM) considers the anisotropic nature of the crystal which is more realistic. It obeys Hooke's law that maintains linear proportionality between strain and stress given by the relation Y = σ/ε, where Y is Young's modulus of elasticity [73]. Assuming small strain in copper nanowires and applying Hooke's law to Eq. (7) yields:

$$\beta_{hkl}cos\theta = \frac{K\lambda}{L} + \frac{4\sigma sin\theta}{Y_{hkl}} \tag{8}$$

The modulus of elasticity (Y_{hkl}) for the cubic crystal system is given by the relation [73]:

$$Y_{hkl} = \left[S_{11} - 2\left[\left(S_{11} - S_{12}\right) - 0.5S_{44}\right]\left\{l_{12}l_{22} + l_{22}l_{32} + l_{32}l_{12}\right\}\right]^{-1} \tag{9}$$

where, S_{11}, S_{12} and S_{44} are elastic compliances of copper with the values 1.5×10^{-11} Pa^{-1}, -0.63×10^{-11} Pa^{-1} and 1.33×10^{-11} Pa^{-1} respectively [73]. Using the above relation, Young's modulus for cubic copper nanowires was calculated as 181.885 GPa. W–H plot was drawn between $\beta_{hkl}\cos\theta$ and $4\sin\theta/Y_{hkl}$ as shown in Fig. 7c. The y-intercept of the linear fit was used to determine the crystallite size of the nanowires using the relation L = kλ/intercept and uniform deformation stress was equal to the slope of the fitted line.

The uniform deformation energy density model (UDEDM) is used to determine energy density of the crystal assuming the crystal to be homogenous and anisotropic in nature. The UDEDM is the best model to determine the crystallite size of metallic samples with cubic structure [74]. Hooke's law relates the energy density (u) and strain as $u = \varepsilon^2 Y_{hkl}/2$ [75]. On substituting ε in terms of u in Eq. (7), we get,

$$\beta_{hkl}cos\theta = \frac{K\lambda}{L} + 4\sin\theta\left(\frac{2u}{Y_{hkl}}\right)^{1/2} \tag{10}$$

W–H plot was drawn between $\beta_{hkl}\cos\theta$ and $4\sin\theta$ $(2/Y_{hkl})^{1/2}$ as shown in Fig. 7d. The y-intercept of the linear fit was used to estimate the crystallite size using the relation L = kλ/intercept and energy density was equal to the square of the slope of the fitted line. Using the relation $u = \varepsilon^2 Y_{hkl}/2$ and σ = εY, the expression for stress comes out to be $\sigma = (2uY_{hkl})^{1/2}$.

The crystallite size, strain, lattice stress and energy density of copper nanowires calculated using UDM, USDM and UDEDM models was summarized in Table 2. As per our knowledge, a comprehensive study using these models on Cu nanowires synthesized using polycarbonate TEM is not yet reported. The study divulges the importance of these models in the determination of crystallite size of copper nanowires.

3.4 Electrical studies

I–V characteristics (IVC) of copper nanostructures obtained from different aqueous citrate baths were measured using Keithley 2400 series source meter. The IVC was measured while the nanostructures were embedded in the membrane to limit their oxidation from the external environment. As discussed earlier, in two electrode IVC measurement, the copper substrate acted as one electrode and the tungsten tip of diameter around 10 μm which covered around 300 nanowires at a time acted as another electrode. The IVC corresponded to the combined and average effect of 300 nanowires assembled parallel to each other inside the polycarbonate

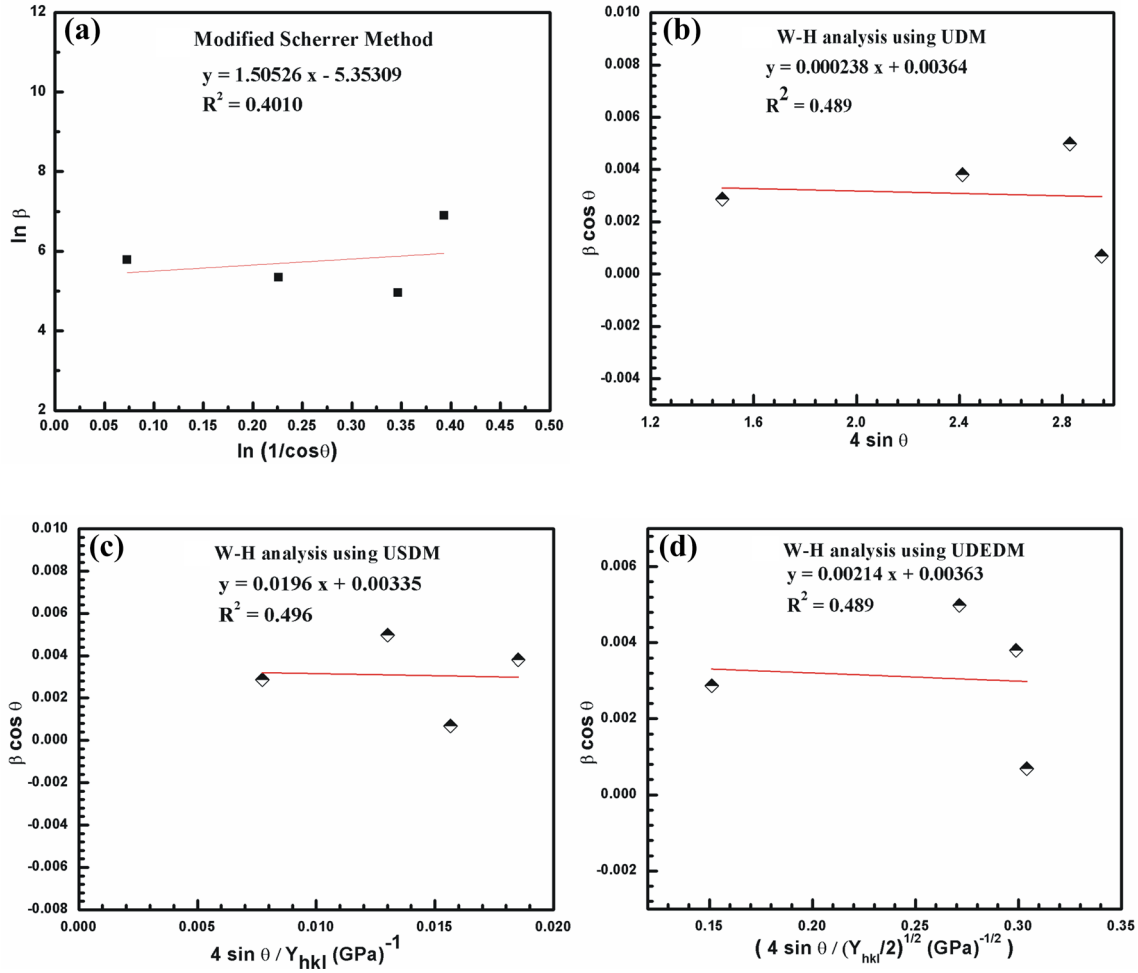

Fig. 7 **a** Modified Scherrer equation of Cu nanowires obtained at pH 1.7. The W–H analysis of Cu nanowires obtained at pH 1.7 assuming **b** UDM; **c** USDM and **d** UDEDM

Table 2 Geometrical parameters of copper nanowires obtained at pH 1.7

Scherrer method	Williamson–Hall method							
	UDM		USDM			UDEDM		
L (nm)	L (nm)	$\varepsilon \times 10^{-3}$	L (nm)	$\varepsilon \times 10^{-3}$	σ (MPa)	L (nm)	$\varepsilon \times 10^{-3}$	u (kJ m^{-3})
29	38	0.238	41	0.107	19.60	38	0.224	4.58

membrane at different places. I–V plot was not obtained for nanowires formed at pH 0.8–1.4, as the deposition was incomplete and as such the electrode tip may not be in contact with all the nanowires. The nanowires obtained at pH 1.7 were complete in length thus making a link between both the electrodes and giving a straight line (Fig. 8a) IVC. The electrical conductivity (σ) of 100 nm nanowires obtained at pH 1.7 was calculated using the formula [76, 77]:

$$\sigma = \frac{L}{R \times A} = \frac{dI}{dV} \times \frac{L}{A} \tag{11}$$

where L is the length of the nanowire, A is the area of the cross-section of cylindrical nanowire and R is the resistance of nanowire calculated from the slope of the linear best fit line. The electrical conductivity of 300 copper nanowires of 100 nm diameter was calculated to be around $4.55 \times 10^6/\Omega$ m while it is $59.6 \times 10^6/\Omega$ m for the bulk copper material. The electrical conductivity of copper nanowires was observed to decrease around 13 times as we advanced from bulk to nanoscale. The electrical conductivity of nanowires depends upon electron–electron interaction, electron–phonon interaction and scattering from surface and grain boundaries

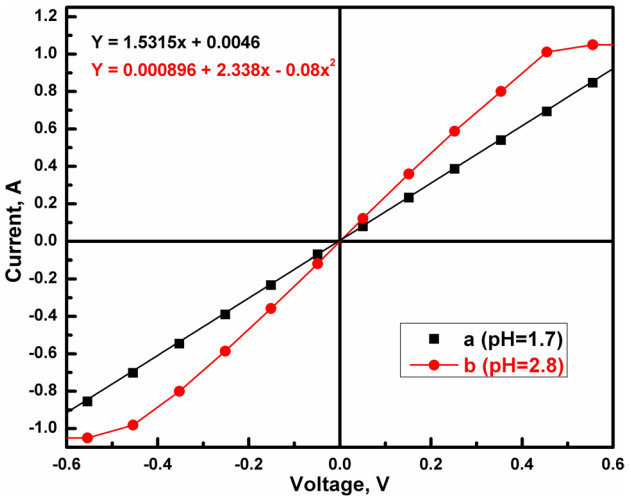

Fig. 8 IVC of the nanowires obtained at pH **a** 1.7 representing linear characteristics **b** 2.8 representing non-ohmic characteristics

[77–83]. The electron transport in low dimensional structures occurs via ballistic and diffusive transport [84, 85]. When the diameter of nanowires is of the order of the electron Fermi wavelength, which is nearly few tenths of nanometer for noble metals, the ballistic transport phenomenon was observed but the nanowires in our case lie the diffusive transport regime, where conduction was caused by charge carriers due to lattice vibration, scattering from external surface of nanowires, grain boundaries and background scattering. The IVC for copper nanowires obtained at pH 2.8 was a non-linear curve (Fig. 8b) due to the formation of copper oxide.

3.5 Field emission studies

The optimized copper nanowires, owing to their high aspect ratio, vertical geometry and high conductivity are excellent candidates for field emission. To investigate the field emission characteristics, we performed Field emission experiments in a vacuum chamber with the pressure maintained at ~ 2×10^{-5} Torr. The experiments were carried out using parallel plate geometry. Plated Au was deployed as the anode and copper nanowires on copper tape were used as the cathode. The separation distance between the top of Cu nanowires and plated Au was maintained at ~ 300 µm as shown in schematic in Fig. 9a. A curve tracer was used for supplying the voltage between the cathode and the anode and also for recording the I–V measurements. As is evident from Fig. 9b these nanowires show extremely low turn-on electric field. This extremely low value of turn on can be attributed to the geometry of these nanowires with sharp edges and corners and high

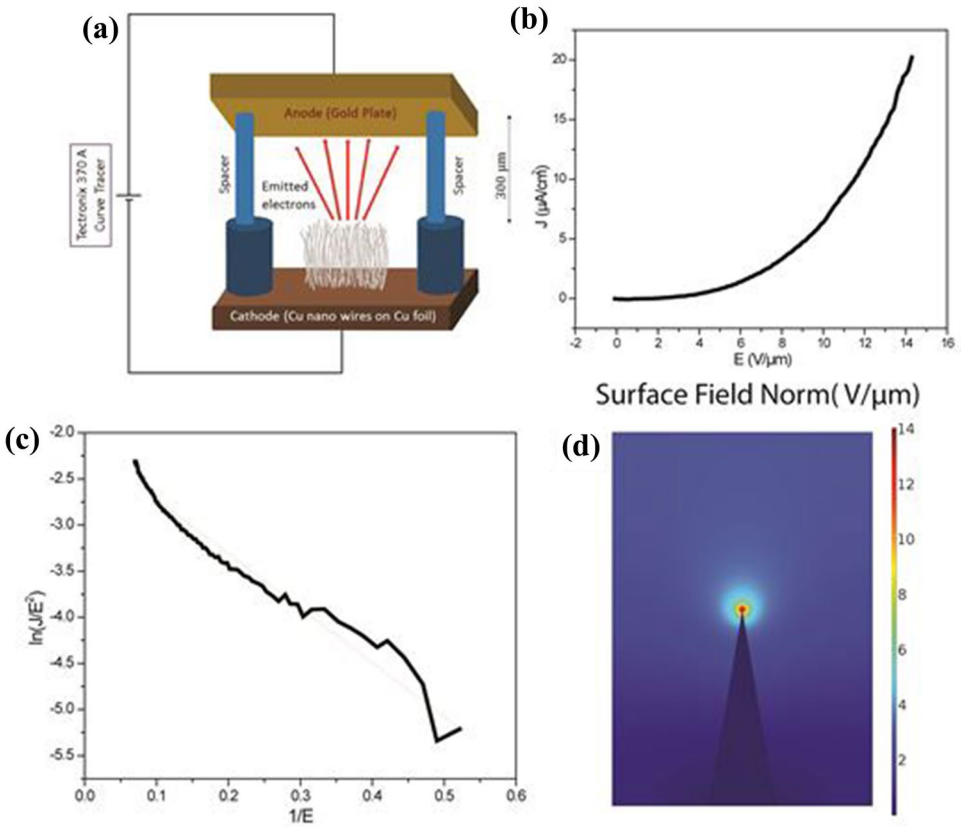

Fig. 9 Field-emission from Cu nanowires. **a** Schematic of field emission with Cu nanowire. **b** *J–E* characteristics of Cu nanowires. **c** F–N plots obtained from the corresponding *J–E* curves. **d** 2D electrostatic field simulations of the Cu nanowires showing field enhancement at the tips

aspect ratio and dense packing leading to the increase in density of sites for field emission. COMSOL simulations were done to look into the electric field distributions in the vicinity of the copper nanowires oriented vertically. The results indicate significant enhancements in the local electric field at the edges and corners of these nanowires (Fig. 9d). To further investigate and analyze the field emission data, we use the Fowler–Nordheim (F–N) equation [57].

$$J = \frac{A\beta^2 E^2}{\phi} \exp\left(-\frac{B\phi^{\frac{3}{2}}}{\beta E}\right)$$

where J is the current density, E is the electric field, ϕ is the work function, β is the electric field enhancement factor and A and B are constants ($A = 1.56 \times 10^{-6}$ eV, $B = 6.83 \times 10^3$ V μm^{-1} $eV^{-3/2}$). From the F–N curve (Fig. 9c) we estimate a very large field-enhancement factor of ~ 10,855 for the Cu nanowire, indicating their outstanding potential as efficient field-emitters for flat panel displays.

4 Conclusions

This paper presents investigations on the effect of pH on the deposition rate and structural composition of Cu nanowires synthesized in polycarbonate TEM by electrochemical method. The pH of the aqueous citrate bath was varied between 0.8 and 2.8 keeping all other deposition parameters constant. For pH 0.8–1.4, nanowires deposited show incomplete deposition in the pores of the membrane whereas an increase in the length of the nanowires was observed with increase in pH. Corresponding to pH 1.7, the nanowires are densely stacked, vertically aligned and possess an average diameter of 105 nm. Further, on increasing the pH value to 2.8 overdeposition in the form of caps was observed at the top of nanowires. From the EDS spectrum of nanowires synthesized at pH 1.7 the wt.% of copper was found to be 97.9% along with a very little oxygen percentage of around 2.02%. XRD spectra confirmed the face centered cubic crystal system for nanowires synthesized at all pH values. The parameters like crystallite size, strain, lattice stress and energy density were calculated for nanowires obtained at pH 1.7. The analysis was done on the basis of Bragg peak broadening of each diffraction peak. The average value of diameter for nanowires obtained at pH 1.7 was found to be ~ 105 nm using SEM analysis. The crystallite size is found to be ca. 38 nm as calculated from W–H (UDEDM) method. I–V characteristic studies have suggested that nanowires obtained at pH 1.7 showed ohmic behavior whereas that obtained at pH 2.8 represented non- linear IVC due to the formation of copper oxide at pH 2.8. We estimate a very large field-enhancement factor of ~ 10,855 for the Cu nanowire at pH 1.7, indicating their outstanding potential as efficient field-emitters for flat panel displays. This research optimizes the parameters viz. electrolytic composition, pH value, temperature etc. for given TEM pore size to get the best yields for the quality of nanowires. The large field-enhancement factor makes them a potential candidate for their application as field emitters, transparent contacts and interconnects in nanoscale devices.

Acknowledgements One of the authors, Dr. Rajesh Kumar is grateful to University Grants Commission (UGC), Govt. of India, New Delhi, India, for providing financial assistance as Raman Post-Doctoral Fellow (F.No. 5-150 /2016(IC)) at Rensselaer Polytechnic Institute, New York, USA. We would also like to take the opportunity to thank all the reviewers for their effort and expertise in reviewing this paper that has helped in further improving the quality of the research paper.

References

1. C. Ross, P.M.R. Media, Annu. Rev. Mater. Res. **31**, 203–235 (2001). https://doi.org/10.1146/annurev.matsci.31.1.203
2. J.M. Krans, J.M. van Ruitenbeek, V.V. Fisun, I.K. Yanson, L.J. de Jongh, The signature of conductance quantization in metallic point contacts. Nature **375**, 767–769 (1995). https://doi.org/10.1038/375767a0
3. M.G. Bawendi, M.L. Steigerwald, L.E. Brus, The quantum mechanics of larger semiconductor clusters ("quantum dots"). Annu. Rev. Phys. Chem. **41**, 477–496 (1990). https://doi.org/10.1146/annurev.pc.41.100190.002401
4. B. Liu, H.C. Zeng, Hydrothermal synthesis of ZnO nanorods in the diameter regime of 50 nm. J. Am. Chem. Soc. **125**, 4430–4431 (2003). https://doi.org/10.1021/ja0299452
5. N. Sanpo, J. Wang, C.C. Berndt, Sol–gel synthesized copper-substituted cobalt ferrite nanoparticles for biomedical applications. J. Nano Res. **22**, 95–106 (2013). https://doi.org/10.4028/www.scientific.net/JNanoR.22.95
6. R.V. Kumar, Y. Diamant, A. Gedanken, Sonochemical synthesis and characterization of nanometer-size transition metal oxides from metal acetates. Chem. Mater. **12**, 2301–2305 (2000). https://doi.org/10.1021/cm000166z
7. A.A. Noyan, A.P. Leontiev, M.V. Yakovlev, I.V. Roslyakov, G.A. Tsirlina, K.S. Napolskii, Electrochemical growth of nanowires in anodic alumina templates: the role of pore branching. Electrochim. Acta **226**, 60–68 (2017). https://doi.org/10.1016/j.electacta.2016.12.142
8. P.G. Schiavi, P. Altimari, A. Rubino, F. Pagnanelli, Electrodeposition of cobalt nanowires into alumina templates generated by one-step anodization. Electrochim. Acta **259**, 711–722 (2018). https://doi.org/10.1016/j.electacta.2017.11.035
9. L. Thiebaud, S. Legeai, J. Ghanbaja, N. Stein, Electrodeposition of high aspect ratio single crystalline tellurium nanowires from piperidinium-based ionic liquid. Electrochim. Acta **222**, 528–534 (2016). https://doi.org/10.1016/j.electacta.2016.11.005
10. C. Zhu, M.J. Panzer, Synthesis of Zn:Cu_2O thin films using a single step electrodeposition for photovoltaic applications. ACS Appl. Mater. Interfaces **7**, 5624–5628 (2015). https://doi.org/10.1021/acsami.5b00643
11. Y. Yang, Y. Chen, F. Liu, X. Chen, Y. Wu, Template-based fabrication and electrochemical performance of CoSb nanowire

arrays. Electrochim. Acta **56**, 6420–6425 (2011). https://doi.org/10.1016/j.electacta.2011.05.011
12. A. Biswas, I.S. Bayer, A.S. Biris, T. Wang, E. Dervishi, F. Faupel, Advances in top–down and bottom–up surface nanofabrication: techniques, applications & future prospects. Adv. Colloid Interface Sci. **170**, 2–27 (2012). https://doi.org/10.1016/j.cis.2011.11.001
13. W. Lu, C.M. Lieber, Nanoelectronics from the bottom up. Nat. Mater. **6**, 841–850 (2007). https://doi.org/10.1038/nmat2028
14. D. Mijatovic, J.C.T. Eijkel, A. van den Berg, Technologies for nanofluidic systems: top–down vs. bottom–up—a review. Lab Chip **5**, 492 (2005). https://doi.org/10.1039/b416951d
15. A. Umer, S. Naveed, N. Ramzan, M.S. Rafique, Selection of a suitable method for the synthesis of copper nanoparticles. Nano **7**, 1230005 (2012). https://doi.org/10.1142/S1793292012300058
16. J. Hu, T.W. Odom, C.M. Lieber, chemistry and physics in one dimension: synthesis and properties of nanowires and nanotubes. Acc. Chem. Res. **32**, 435–445 (1999). https://doi.org/10.1021/ar9700365
17. C. Thelander, P. Agarwal, S. Brongersma, J. Eymery, L.F. Feiner, A. Forchel, M. Scheffler, W. Riess, B.J. Ohlsson, U. Gösele, L. Samuelson, Nanowire-based one-dimensional electronics. Mater. Today **9**, 28–35 (2006). https://doi.org/10.1016/S1369-7021(06)71651-0
18. N.I. Kovtyukhova, B.R. Martin, J.K.N. Mbindyo, P.A. Smith, B. Razavi, T.S. Mayer, T.E. Mallouk, Layer-by-layer assembly of rectifying junctions in and on metal nanowires. J. Phys. Chem. B **105**, 8762–8769 (2001). https://doi.org/10.1021/jp010867z
19. C. Martin-Olmos, H.I. Rasool, B.H. Weiller, J.K. Gimzewski, Graphene MEMS: AFM probe performance improvement. ACS Nano **7**, 4164–4170 (2013). https://doi.org/10.1021/nn400557b
20. E. Cruz-Silva, F. López-Urías, E. Muñoz-Sandoval, B.G. Sumpter, H. Terrones, J.-C. Charlier, V. Meunier, M. Terrones, Electronic transport and mechanical properties of phosphorus- and phosphorus–nitrogen-doped carbon nanotubes. ACS Nano **3**, 1913–1921 (2009). https://doi.org/10.1021/nn900286h
21. J.Y. Oh, Y.S. Kim, Y. Jung, S.J. Yang, C.R. Park, Preparation and exceptional mechanical properties of bone-mimicking size-tuned graphene oxide@carbon nanotube hybrid paper. ACS Nano **10**, 2184–2192 (2016). https://doi.org/10.1021/acsnano.5b06719
22. Z. Li, Q. Guo, Z. Li, G. Fan, D.-B. Xiong, Y. Su, J. Zhang, D. Zhang, enhanced mechanical properties of graphene (reduced graphene oxide)/aluminum composites with a bioinspired nanolaminated structure. Nano Lett. **15**, 8077–8083 (2015). https://doi.org/10.1021/acs.nanolett.5b03492
23. F. Xiong, H. Wang, X. Liu, J. Sun, M. Brongersma, E. Pop, Y. Cui, Li intercalation in MoS_2: in situ observation of its dynamics and tuning optical and electrical properties. Nano Lett. **15**, 6777–6784 (2015). https://doi.org/10.1021/acs.nanolett.5b02619
24. R. Yan, J.R. Simpson, S. Bertolazzi, J. Brivio, M. Watson, X. Wu, A. Kis, T. Luo, A.R. Hight Walker, H.G. Xing, Thermal conductivity of monolayer molybdenum disulfide obtained from temperature-dependent raman spectroscopy. ACS Nano **8**, 986–993 (2014). https://doi.org/10.1021/nn405826k
25. M. Rani, R. Kumar, Rajesh Kumar, R. Singh, S.K. Chakarvarti, Preparation and characterization of Ag_2Se nanowalled tubules by electrochemical method. Chalcogenide Lett. **10**, 99–104 (2013)
26. C. Tazlaoanu, L. Ion, I. Enculescu, M. Sima, M. Enculescu, E. Matei, R. Neumann, R. Bazavan, D. Bazavan, S. Antohe, Transport properties of electrodeposited ZnO nanowires. Phys. E Low Dimens. Syst. Nanostruct. **40**, 2504–2507 (2008). https://doi.org/10.1016/j.physe.2007.07.013
27. S. Öztürk, N. Klnç, N. Taşaltn, Z.Z. Öztürk, Fabrication of ZnO nanowires and nanorods. Phys. E Low Dimens. Syst. Nanostruct. **44**, 1062–1065 (2012). https://doi.org/10.1016/j.physe.2011.01.015
28. P.S. Chinthamanipeta, Q. Lou, D.A. Shipp, Periodic titania nanostructures using block copolymer templates. ACS Nano **5**, 450–456 (2011). https://doi.org/10.1021/nn102207y
29. P. Enzel, J.J. Zoller, T. Bein, Intrazeolite assembly and pyrolysis of polyacrylonitrile. J. Chem. Soc. Chem. Commun. **8**, 633–635 (1992)
30. C. Guerret-Piecourt, Y. Le Bouar, A. Loiseau, H. Pascard, Relation between metal electronic structure and morphology of metal compounds inside carbon nanotubes. Nature **372**, 761–765 (1994)
31. C.M. Bruinink, M. Péter, P.A. Maury, M. de Boer, L. Kuipers, J. Huskens, D.N. Reinhoudt, Capillary force lithography: fabrication of functional polymer templates as versatile tools for nanolithography. Adv. Funct. Mater. **16**, 1555–1565 (2006). https://doi.org/10.1002/adfm.200500629
32. A. Sharma, A. Srivastava, Y. Jeon, B. Ahn, Template-assisted fabrication of nanostructured tin (β-Sn) arrays for bulk microelectronic packaging devices. Metals **8**, 347 (2018). https://doi.org/10.3390/met8050347
33. H. Shang, G. Cao, Template-based synthesis of nanorod or nanowire arrays, in *Springer Handbook of Nanotechnology* (Springer, Berlin, 2010), pp. 169–186
34. J.B. Mohler, H.J. Sedusky, *Electroplating for the Metallurgist, Engineer and Chemist* (Chemical Publishing, New York, 1951)
35. F.R.N. Nabarro, P.J. Jackson, Growth of crystal whiskers—a review, in *Growth and Perfection of Crystals*, ed. by R.H. Doremus, B.W. Roberts, D. Turnbull (Wiley, New York, 1958), pp. 11–102
36. B.Z. Tang, H. Xu, Preparation, alignment and optical properties of soluble poly(phenylacetylene)-wrapped carbon nanotubes. Macromolecules **32**, 2567–2569 (1999)
37. G.E. Possin, A method for forming very small diameter wires. Rev. Sci. Instrum. **41**, 772–774 (1970)
38. W.D. Williams, N. Giordano, Fabrication of 80 Å metal wires. Rev. Sci. Instrum. **55**, 410–412 (1984)
39. T.M. Whitney, J.S. Jiang, P.C. Searson, C.L. Chien, Fabrication and magnetic properties of arrays of metallic nanowires. Science **261**, 1316–1319 (1993)
40. S. Ding, J. Jiu, Y. Tian, T. Sugahara, S. Nagao, K. Suganuma, Fast fabrication of copper nanowire transparent electrodes by a high intensity pulsed light sintering technique in air. Phys. Chem. Chem. Phys. **17**, 31110–31116 (2015). https://doi.org/10.1039/C5CP04582G
41. B.C. Ranu, R. Dey, T. Chatterjee, S. Ahammed, Copper nanoparticle-catalyzed carbon-carbon and carbon-heteroatom bond formation with a greener perspective. ChemSusChem **5** (2012) 22–44. https://doi.org/10.1002/cssc.201100348
42. S.E. Allen, R.R. Walvoord, R. Padilla-Salinas, M.C. Kozlowski, Aerobic copper-catalyzed organic reactions. Chem. Rev. **113**, 6234–6458 (2013). https://doi.org/10.1021/cr300527g
43. Z.-Y. Shih, A.P. Periasamy, P.-C. Hsu, H.-T. Chang, Synthesis and catalysis of copper sulfide/carbon nanodots for oxygen reduction in direct methanol fuel cells. Appl. Catal. B Environ. **132–133**, 363–369 (2013). https://doi.org/10.1016/j.apcatb.2012.12.004
44. R. Kaur, B. Pal, Cu nanostructures of various shapes and sizes as superior catalysts for nitro-aromatic reduction and co-catalyst for Cu/TiO_2 photocatalysis. Appl. Catal. A Gen. **491**, 28–36 (2015). https://doi.org/10.1016/j.apcata.2014.10.035
45. R.C. Pawar, D.H. Choi, J.S. Lee, C.S. Lee, Formation of polar surfaces in microstructured ZnO by doping with Cu and applications in photocatalysis using visible light. Mater. Chem. Phys. **151**, 167–180 (2015). https://doi.org/10.1016/j.matchemphys.2014.11.051
46. S.M. Bergin, Y.H. Chen, A.R. Rathmell, P. Charbonneau, Z.Y. Li, B.J. Wiley, The effect of nanowire length and diameter on the

properties of transparent, conducting nanowire films. Nanoscale **4**, 1996 (2012). https://doi.org/10.1039/c2nr30126a
47. G.H. Chan, J. Zhao, E.M. Hicks, G.C. Schatz, R.P. Van Duyne, Plasmonic properties of copper nanoparticles fabricated by nanosphere lithography. Nano Lett. **7**, 1947–1952 (2007). https://doi.org/10.1021/nl070648a
48. K.A. Dean, A new era: nanotube displays. Nat. Photonics **1**, 273–275 (2007). https://doi.org/10.1038/nphoton.2007.64
49. A.H. Li, S.H. Cheng, H.D. Li, Q. Yu, J.W. Liu, X.Y. Lv, Effect of nitrogen on deposition and field emission properties of boron-doped micro- and nano-crystalline diamond films. Nano Micro Lett. **2**, 154–159 (2010). https://doi.org/10.5101/nml.v2i3.p154-159
50. K.B.K. Teo, M. Chhowalla, G.A.J. Amaratunga, W.I. Milne, G. Pirio, P. Legagneux, F. Wyczisk, D. Pribat, D.G. Hasko, Field emission from dense, sparse, and patterned arrays of carbon nanofibers. Appl. Phys. Lett. **80**, 2011–2013 (2002). https://doi.org/10.1063/1.1461868
51. B.K. Sarker, S.I. Khondaker, Thermionic emission and tunneling at carbon nanotube–organic semiconductor interface. ACS Nano **6**, 4993–4999 (2012). https://doi.org/10.1021/nn300544v
52. L. Li, X. Fang, H.G. Chew, F. Zheng, T.H. Liew, X. Xu, Y. Zhang, S. Pan, G. Li, L. Zhang, Crystallinity-controlled germanium nanowire arrays: potential field emitters. Adv. Funct. Mater. **18**, 1080–1088 (2008). https://doi.org/10.1002/adfm.200701051
53. D. Ye, S. Moussa, J.D. Ferguson, A.A. Baski, M.S. El-Shall, Highly efficient electron field emission from graphene oxide sheets supported by nickel nanotip arrays. Nano Lett. **12**, 1265–1268 (2012). https://doi.org/10.1021/nl203742s
54. S. Ramanathan, Y. Chen, Y. Tzeng, Zinc oxide nanowire-based field emitters. Phys. E Low Dimens. Syst. Nanostruct. **43**, 285–288 (2010). https://doi.org/10.1016/j.physe.2010.07.072
55. J. Joo, S.J. Lee, D.H. Park, Y.S. Kim, Y. Lee, C.J. Lee, S.R. Lee, Field emission characteristics of electrochemically synthesized nickel nanowires with oxygen plasma post-treatment. Nanotechnology **17**, 3506–3511 (2006). https://doi.org/10.1088/0957-4484/17/14/024
56. C. Chang, T.K. Huang, H.K. Lin, Y.F. Tzeng, C.W. Peng, F.M. Pan, C.Y. Lee, H.T. Chiu, Growth of pagoda-topped tetragonal copper nanopillar arrays. ACS Appl. Mater. Interfaces **1**, 1375–1378 (2009). https://doi.org/10.1021/am900264u
57. J. Zhou, N.S. Xu, S.Z. Deng, J. Chen, J.C. She, Z.L. Wang, Large-area nanowire arrays of molybdenum and molybdenum oxides: synthesis and field emission properties. Adv. Mater. **15**, 1835–1840 (2003). https://doi.org/10.1002/adma.200305528
58. S. Wang, Y. He, X. Fang, J. Zou, Y. Wang, H. Huang, P.M.F.J. Costa, M. Song, B. Huang, C.T. Liu, P.K. Liaw, Y. Bando, D. Golberg, Structure and field-emission properties of sub-micrometer-sized tungsten-whisker arrays fabricated by vapor deposition. Adv. Mater. **21**, 2387–2392 (2009). https://doi.org/10.1002/adma.200803401
59. W.A. Deheer, W.S. Bacsa, A. Chatelain, T. Gerfin, R. Humphrey-Baker, L. Forro, D. Ugarte, Aligned carbon nanotube films: production and optical and electronic properties. Science **268**, 845–847 (1995). https://doi.org/10.1126/science.268.5212.845
60. E.M. Garcia, J.S. Santos, E.C. Pereira, M.B.J.G. Freitas, Electrodeposition of cobalt from spent Li–ion battery cathodes by the electrochemistry quartz crystal microbalance technique. J. Power Sources **185**, 549–553 (2008). https://doi.org/10.1016/j.jpowsour.2008.07.011
61. T. Gandhi, K.S. Raja, M. Misra, Synthesis of ZnTe nanowires onto TiO_2 nanotubular arrays by pulse-reverse electrodeposition. Thin Solid Films **517**, 4527–4533 (2009). https://doi.org/10.1016/j.tsf.2008.12.046
62. M. Tagliazucchi, I. Szleifer, Transport mechanisms in nanopores and nanochannels: can we mimic nature? Mater. Today **18**, 131–142 (2015). https://doi.org/10.1016/j.mattod.2014.10.020
63. J. Vazquez-Arenas, L. Altamirano-Garcia, T. Treeratanaphitak, M. Pritzker, R. Luna-Sánchez, R. Cabrera-Sierra, Co–Ni alloy electrodeposition under different conditions of pH, current and composition. Electrochim. Acta **65**, 234–243 (2012). https://doi.org/10.1016/j.electacta.2012.01.050
64. T. Mahalingam, C. Sanjeeviraja, S. Esther Dali, M. Jayachandran, M.J. chockalingam, Galvanostatic deposition of Cu_2O layers through the electrogeneration of base route. J. Mater. Sci. Lett. **17**, 603–605 (1998). https://doi.org/10.1023/A:1006594225339
65. P.E. de Jongh, D. Vanmaekelbergh, J.J. Kelly, Cu_2O: electrodeposition and characterization. Chem. Mater. **11**, 3512–3517 (1999). https://doi.org/10.1021/cm991054e
66. E.W. Bohannan, M.G. Shumsky, J.A. Switzer, Epitaxial electrodeposition of copper(I) oxide on single-crystal gold (100). Chem. Mater. **11**, 2289–2291 (1999). https://doi.org/10.1021/cm990304o
67. R.K. Dhillon, P. Singh, S.K. Gupta, S. Singh, R. Kumar, Study of high energy (MeV) N^{6+} ion and gamma radiation induced modifications in low density polyethylene (LDPE) polymer. Nucl. Instrum. Methods Phys. Res. Sect. B Beam Interact. Mater. Atoms **301**, 12–16 (2013). https://doi.org/10.1016/j.nimb.2013.02.014
68. M.K. Jaiswal, D. Kanjilal, R. Kumar, Structural and optical studies of 100 MeV Au irradiated thin films of tin oxide. Nucl. Instrum. Methods Phys. Res. Sect. B Beam Interact. Mater. Atoms **314**, 170–175 (2013). https://doi.org/10.1016/j.nimb.2013.05.053
69. R. Kumar, P. Singh, S.K. Gupta, R. Gupta, M.K. Jaiswal, M. Prasad, A. Roychowdhury, R.P. Chauhan, D. Das, Radiation induced nano-scale free volume modifications in amorphous polymeric material: a study using positron annihilation lifetime spectroscopy. J. Radioanal. Nucl. Chem. **314**, 1659–1666 (2017). https://doi.org/10.1007/s10967-017-5510-9
70. S.K. Gupta, R. Gupta, P. Singh, V. Kumar, M.K. Jaiswal, S.K. Chakarvarti, R. Kumar, Modifications in physico-chemical properties of 100 MeV oxygen ions irradiated polyimide Kapton-H polymer. Nucl. Instrum. Methods Phys. Res. Sect. B Beam Interact. Mater. Atoms. **406**, 188–192 (2017). https://doi.org/10.1016/j.nimb.2017.02.011
71. S. Goel, N. Sinha, H. Yadav, A.J. Joseph, B. Kumar, Experimental investigation on the structural, dielectric, ferroelectric and piezoelectric properties of La doped ZnO nanoparticles and their application in dye-sensitized solar cells. Phys. E Low Dimens. Syst. Nanostruct. **91**, 72–81 (2017). https://doi.org/10.1016/j.physe.2017.04.010
72. S. Goel, N. Sinha, H. Yadav, S. Godara, A.J. Joseph, B. Kumar, Ferroelectric Gd-doped ZnO nanostructures: enhanced dielectric, ferroelectric and piezoelectric properties. Mater. Chem. Phys. **202**, 56–64 (2017). https://doi.org/10.1016/j.matchemphys.2017.08.067
73. W.H. Chen, H.C. Cheng, C.F. Yu, The mechanical, thermodynamic, and electronic properties of cubic Au_4Al crystal via first-principles calculations. J. Alloys Compd. **689**, 857–864 (2016). https://doi.org/10.1016/j.jallcom.2016.08.050
74. V. Mote, Y. Purushotham, B. Dole, Williamson–Hall analysis in estimation of lattice strain in nanometer-sized ZnO particles. J. Theor. Appl. Phys. **6**, 6 (2012). https://doi.org/10.1186/2251-7235-6-6
75. H. Yadav, N. Sinha, S. Goel, B. Kumar, Eu-doped ZnO nanoparticles for dielectric, ferroelectric and piezoelectric applications. J. Alloys Compd. **689**, 333–341 (2016). https://doi.org/10.1016/j.jallcom.2016.07.329
76. C. Narula, R.P. Chauhan, High dose gamma ray exposure effect on the properties of CdSe nanowires. Radiat. Phys. Chem. **144**, 405–412 (2017). https://doi.org/10.1016/j.radphyschem.2017.10.003

77. Rashi Gupta, R.P. Chauhan, S.K. Chakarvarti, Rajesh Kumar, Gamma ray induced modifications in copper microwires synthesized using track-etched membrane. Vacuum **148**, 239–247 (2018). https://doi.org/10.1016/j.vacuum.2017.11.031
78. A. Khorsand Zak, W.H. Abd. M.E. Majid, R. Abrishami, Yousefi, X-ray analysis of ZnO nanoparticles by Williamson–Hall and size–strain plot methods. Solid State Sci. **13**, 251–256 (2011). https://doi.org/10.1016/j.solidstatesciences.2010.11.024
79. E.H. Sondheimer, The mean free path of electrons in metals. Adv. Phys. **1**, 1–42 (1952). https://doi.org/10.1080/00018735200101151
80. K. Barmak, A. Darbal, K.J. Ganesh, P.J. Ferreira, J.M. Rickman, T. Sun, B. Yao, A.P. Warren, K.R. Coffey, Surface and grain boundary scattering in nanometric Cu thin films: a quantitative analysis including twin boundaries. J. Vac. Sci. Technol. A Vac Surf. Film **32**, 61503 (2014). https://doi.org/10.1116/1.4894453
81. A.F. Mayadas, M. Shatzkes, Electrical-resistivity model for polycrystalline films: the case of arbitrary reflection at external surfaces. Phys. Rev. B **1**, 1382–1389 (1970). https://doi.org/10.1103/PhysRevB.1.1382
82. Y. Kitaoka, T. Tono, S. Yoshimoto, T. Hirahara, S. Hasegawa, T. Ohba, Direct detection of grain boundary scattering in damascene Cu wires by nanoscale four-point probe resistance measurements. Appl. Phys. Lett. **95**, 52110 (2009). https://doi.org/10.1063/1.3202418
83. Q. Huang, C.M. Lilley, M. Bode, R. Divan, Surface and size effects on the electrical properties of Cu nanowires. J. Appl. Phys. **104**, 23709 (2008). https://doi.org/10.1063/1.2956703
84. Rashi Gupta, R.P. Chauhan, S.K. Chakarvarti, Rajesh Kumar, Effect of SHI on properties of template synthesized Cu nanowires. Ionics **24**, 1–12 (2018). https://doi.org/10.1007/s11581-018-2578-3
85. J. Homoth, M. Wenderoth, T. Druga, L. Winking, R.G. Ulbrich, C. Bobisch, B. Weyers, A. Bannani, E. Zubkov, a M. Bernhart, M.R. Kaspers, R. Möller, Electronic transport on the nanoscale: ballistic transmission and Ohm's law. Nano Lett. **9**, 1588–1592 (2009). https://doi.org/10.1021/nl803783g